

Effect of Geometrical Modeling on Prediction of Laser-Induced Heat Transfer in Metal Foam

Tizian Bucher¹

Advanced Manufacturing Laboratory
Department of Mechanical Engineering
Columbia University
New York, NY 10027
e-mail: tb2430@columbia.edu
ASME Member

Christopher Bolger

Advanced Manufacturing Laboratory
Department of Mechanical Engineering
Columbia University
New York, NY 10027
e-mail: cdb2156@columbia.edu

Min Zhang

Laser Processing Research Center
School of Mechanical and Electrical Engineering
Soochow University
Suzhou, Jiangsu 215021, China
e-mail: mzhang@aliyun.com
ASME Member

Chang Jun Chen

Laser Processing Research Center
School of Mechanical and Electrical Engineering
Soochow University
Suzhou, Jiangsu 215021, China
e-mail: chjchen2001@aliyun.com
ASME Member

Y. Lawrence Yao

Advanced Manufacturing Laboratory
Department of Mechanical Engineering
Columbia University
New York, NY 10027
e-mail: yly1@columbia.edu
ASME Fellow

¹ Corresponding author

ABSTRACT

Over the past several decades, aluminum foam has found increasing popularity in industrial applications due to its unique material properties. Unfortunately, to this day aluminum foam can only be affordably manufactured in flat panels, and it becomes necessary to bend the foam to the final shape that is required in engineering applications. Past studies have shown that thin cell walls crack and collapse when conventional mechanical bending methods are used. Laser forming, on the other hand, was shown to be able to bend the material without causing fractures and cell collapse.

This study was focused on the thermal aspects of laser forming of closed-cell aluminum foam. An infrared camera was used to measure the transient temperature response of aluminum foam to stationary and moving laser sources. Moreover, three different numerical models were developed to determine how much geometrical accuracy is needed to obtain a good agreement with experimental data. Different levels of geometrical complexity were used, including a simple solid geometry, a Kelvin-cell based geometry, and a highly accurate porous geometry that was based on an X-ray computed tomography (CT) scan. The numerical results were validated with the experimental data, and the performances of the numerical models were compared.

Keywords: Laser Forming, Metal Foam, Geometrical Modeling, Heat Transfer, Numerical Simulation

1. INTRODUCTION

Aluminum-foam (Al-foam) is a relatively new material that has stimulated a lot of interest due to its high strength to weight ratio and its excellent shock and noise absorption properties [1]. Al-foam can be manufactured in many different ways, yet it is most commonly manufactured in flat panels [2]. In many engineering applications such as car bumpers or spacecraft components, however, Al-foam needs to be in specific shapes. Since near-net shape manufacturing is difficult and expensive, it becomes necessary to bend Al-foam to the desired shape. Bending Al-foam is not trivial because the cell walls can only sustain low stresses and crack easily. As a consequence, conventional mechanical bending methods cause fracture and cell collapse [3,4]. Therefore, an alternative bending method is needed.

Laser forming is an alternative advanced manufacturing method used to bend materials. The process is well understood for solid materials, and many aspects of the process have been studied previously. Li et al., for instance, studied laser forming under constant line energy as well as strain rate effects during laser forming [5,6]. Cheng et al. studied cooling effects during multi-scan experiments and microstructural changes in steel during laser forming [7,8]. The laser forming process has also been studied for sheets of varying thicknesses [9], and algorithms have been developed for process synthesis [10].

Previous studies have shown that laser forming can successfully bend metal foams as well. Guglielmotti et al. [11] and Quadrini et al. [12] investigated the feasibility of laser forming of Al-foam sandwich panels and open-cell Al-foams for different power levels, scanning speeds, sheet thicknesses and foam densities. They found that laser forming of Al-foam is possible without cell collapse and skin delamination. The maximum number of scan lines was found to be limited by foam densification, melting, and crack growth on the bottom surface. The optimum processing conditions and the corresponding maximum bending angles were determined. The experimental results were limited to bending angle measurements, and heat transfer issues were not addressed. Moreover, no numerical studies have been performed yet.

Santo et al. [13] and Quadrini et al. [14] extended the previous parametrical study to large-pore open-cell Al-foams. They first introduced numerical schemes that explicitly modeled the foam geometry. Uncoupled sequential thermal and mechanical models were used, and the material data for AlSi7Mg was temperature-dependent. The numerical model was indirectly validated using a 3-point bending test, but no comparison was made between experimental and numerical laser forming results. The heat transfer results were limited to color contour plots and time-history curves at selected points, and no detailed discussion was performed of the underlying heat transfer aspects of laser forming.

In addition, the microstructural changes in Al-foam during laser forming have been studied, as well as the effect of heat treatments on the mechanical properties of Al-

foam [15,16]. Again, no comparison was made between numerical and experimental data, and similar heat transfer results were reported as in the previous studies.

More recently, Zhang et al. used laser forming on closed-cell Al-foam [17]. They developed two types of numerical models in uncoupled thermo-mechanical analyses. The first model assumed a solid geometry and used foam material properties, while the second model used an explicit geometry with solid material properties. The models were employed to analyze both the temperature history during laser scans as well as the mechanical response of the foam during laser forming. Zhang et al. was the first group to compare numerical bending angles with experimentally measured bending angles. However, the heat transfer results of the numerical simulations were not verified experimentally. Moreover, a highly simplified explicit porous model was used, as will be discussed later.

The current study was focused on the heat transfer aspects of laser forming of closed-cell Al-foam that is shown in Fig. 1. While laser forming is a thermo-mechanical process, one may uncouple the thermal process from the mechanical process and use the thermal results as initial conditions for the mechanical analysis. Hence, a good understanding of the heat flow and the transient temperature profiles during laser forming is vital to explain why and under which circumstances foams can bend. Especially from a numerical standpoint, accurate thermal simulations are the key to performing successful mechanical simulations. In order to determine the best way to model Al-foam, several numerical models with different levels of geometrical complexities were compared. The models included an equivalent model with a solid

geometry, a Kelvin-cell model with a Kelvin-cell geometry, and a voxel model with a geometry that was based on an X-ray computed-tomography (CT) scan. The numerical models were then validated by experimental data, which was obtained using an infrared camera to measure the transient response of Al-foam during laser pulses and laser scans.

2. BACKGROUND

2.1 Heat Transfer in Metal Foams

There are four different mechanisms through which heat can be transferred in foams: (1) solid conduction, (2) gas conduction through the cavities, (3) natural convection inside the cavities and (4) radiation heat transfer. Since the thermal conductivities of metals are generally very large, most of the heat transfer occurs through solid conduction. The contribution of gas conduction is generally very small since the gas thermal conductivity is several orders of magnitudes smaller than the solid thermal conductivity. In the current study, the maximum contribution of gas conduction was calculated to be around 0.2%, which is negligible. Natural convection inside the cavities is governed by the Grashof number

$$Gr = \frac{g \beta \Delta T_c d^3 \rho_g^2}{\mu_g^2} \quad (1)$$

where g is the gravitational acceleration, β is the volumetric expansion coefficient of the gas, ΔT_c is the maximum temperature gradient over a single cavity, d is the cavity diameter, ρ_g and μ_g are the density and dynamic viscosity of the gas, respectively. The

Grashof number describes the ratio of buoyant forces to viscous forces. If $Gr < 1000$, viscous forces are dominant over buoyant forces, and natural convection is suppressed [18]. In the current study, the Grashof number was one order of magnitude smaller than the threshold and thus the contribution of natural convection inside the cavities was negligible. Finally, the radiation heat flux in metal foams is governed by a combination of Boltzmann's law and the Beer Lambert law [19]

$$k_{rad} = 4\varepsilon\sigma T_{avg}^3 t e^{-k_s \frac{\rho_f}{\rho_s} t} \quad (2)$$

where ε is the emissivity, σ is the Boltzmann constant, T_{avg} is the average between the top and the bottom surface temperatures, t is the sheet thickness, k_s is the solid thermal conductivity, and ρ_f/ρ_s is the solid volume fraction. In the current study, the maximum contribution of radiative heat transfer was calculated to be around 3% of the total heat transfer. Therefore, radiation had a higher impact than gas conduction and gas convection, but its contribution was still negligible.

2.2 Numerical Models

Numerical simulations of the laser forming process are very powerful since they can determine the best processing parameters without having to perform an excessive amount of experiments. For metal foams, numerical simulations become even more important since foams can have different densities and mass distributions, and thus the number of process parameters is even greater than in solid laser forming.

In this study, three different numerical models were used and are shown in Fig. 2. The first model strove to simulate the complex laser forming process with the simplest

possible model geometry, which is a solid. In the second model, the foam geometry was approximated using a Kelvin-cell geometry, which will be referred to as Kelvin-cell model. The goal was to use an approximate geometry that is easy to generate but still as representative of the actual foam geometry as possible. The third and final model, which will be referred to as voxel model, aimed to replicate the exact foam geometry by using an FEM model that was based on an X-ray computed tomography (CT) scan. The first model is called an equivalent model, while the latter two models fall into the category of explicit porous models.

2.2.1 Equivalent Model

Equivalent models have a solid geometry and use foam material properties. They are rather widely applicable and have been used for different types of laser processes in the past. Mukarami et al. [20], for instance, used an equivalent model for laser welding of porous lotus-type magnesium, and Yilbas et al. [21] used an equivalent model for laser cutting of Al-foam. In both cases, phase changes had to be taken into consideration, which were of no concern in the current study. Moreover, Mukarami et al. used anisotropic material properties due to the elongated shapes of the pores, whereas this study assumed isotropic material behavior. An equivalent model was also used by Zhang et al. to model laser-forming of Al-foam [17]. In their study, however, the solid volume fraction of the Al-foam was more than twice the solid volume fraction of the foam that was used in this study, which was only 11%. This study thus investigated whether even low-density closed-cell foams may be approximated with a solid geometry.

The main challenge associated with equivalent models is the determination of the equivalent material properties. For a heat transfer analysis, three material properties are required: the density, specific heat and thermal conductivity. The density of the foam can be measured, and the equivalent specific heat of the foam is approximately equal to the specific heat of the solid material out of which the foam is made [19-20,22]. The equivalent thermal conductivity, on the other hand, needs to be determined. In most cases, temperature-dependent data only exists for the solid material out of which the foam is made but not for the foam itself. Therefore, it becomes necessary to relate the equivalent thermal conductivity to the corresponding solid thermal conductivity. This can be done with many different methods that are summarized in [23,24]. In this study, three different methods were compared to highlight the important role that foam properties play in equivalent models. In the first two methods, the foam thermal conductivity k_{eq} was related to the solid thermal conductivity k_s through the volume fraction ρ_f/ρ_s and a shape factor f_z :

$$k_{eq} = k_s \frac{\rho_f}{\rho_s} f_z \quad (3)$$

The first method determined the shape factor by assuming that the foam structure may be represented as a Voronoi model with the random morphological microstructure that was proposed by Lu et al. [25]. In the second method, the shape factor was visually determined by measuring the cross-sectional areas A_i and the angular orientations γ_i of the cell walls as shown in Fig. 3 [26]:

$$f_z = \frac{\sum_{i=1}^n A_i \cos^2(\gamma_i)}{\sum_{i=1}^n A_i} \quad (4)$$

Finally, in the third method, experimental laser-forming data was used to tune the equivalent thermal conductivity while all the remaining variables and processing parameters were left constant.

2.2.2 Explicit Porous Models

Explicit porous models use solid material properties and aim to replicate the closed-cell foam geometry. They generally fall into two categories, which may be called approximate models and “exact” CT-based models. Approximate models assume a unit cell geometry and repeat the geometry to generate a full-scale model. Zhang et al., for instance, used spherical unit cells in a closed-packed arrangement to simulate closed-cell Al-foam [17]. While being extremely simple to model, spherical cavity models have the major disadvantage that the minimum volume fraction is limited to 27%. Moreover, they overestimate the material accumulation at cell intersections and underestimate the minimum cell wall thickness. An alternative unit cell geometry is the Kelvin cell, which was used in this study and has also been used for compression and impact tests by De Giorgi et al. [27] and Mills et al [28], respectively. In both studies, the Kelvin-cell model was exclusively used for mechanical analyses, and no thermal simulations were performed. Furthermore, the foam cell wall thicknesses were very thin in both studies, which allowed for the simplification of the geometry by using shell elements. In the current study, however, no such simplifications could be used. De Giorgi et al. also introduced a more sophisticated approximated model that used randomly oriented

ellipsoids of different sizes [27]. The resulting micro-structure was rather close to the real foam, and a good agreement was achieved with experimental compression test data. However, the model required sophisticated algorithms to generate the random geometry, which defeated the original purpose of using an approximated geometry.

The second category of explicit porous models is based on CT-scans. CT-scans use X-rays and can thus measure the internal structure of Al-foam at a high resolution. The result of a CT-scan is a point cloud that gives the attenuation coefficient at every point of the measured object. For aluminum foams that are filled with air cavities, the point cloud contains zeros for air and finite values for aluminum. In order to obtain a FEM model from the CT-scan, the point cloud needs to be translated into a solid geometry. Most commonly, two approaches are used to achieve that. The first approach uses a “marching cube method”, which finds and connects the surfaces between the solid and air [23]. The drawback of this method is that it only generates open surfaces that need to be capped in order to obtain a solid geometry. While this is comparatively easy for open-cell foams, it becomes extremely cumbersome for closed-cell foams that have intricate micro-morphologies. The second method, which was used in this study, simply converts each solid data point of the point cloud into cubical volumes, called voxels. The advantage of this approach is that it is more straightforward to perform and directly generates a solid geometry that can be used in FE software.

The numerical simulations were performed in the commercial FEM software ABAQUS. The governing equation for the numerical simulations was Fourier’s law:

$$q = -k\nabla T \quad (5)$$

Linear 8-node brick elements DC3D8 were used for the equivalent and the voxel model, and linear 4-node tetrahedrons DC3D4 were used for the Kelvin-cell model. For the equivalent model, a refined mesh was used close to the laser scan line to ensure that high temperature gradients could be captured. A FORTRAN subroutine DFLUX was employed to model the Gaussian laser beam. An algorithm was used within the subroutine to adjust the beam radius with varying depth. The absorption coefficient of the model was set equal to the experimentally measured absorption coefficient that will be discussed in Sec. 4.1.

3. EXPERIMENTAL PROCEDURES

Closed-cell Al-foam was used containing 7 weight percent silicon. The foam was manufactured with a melt-foaming method, which used TiH_2 as a foaming agent and Calcium to increase the viscosity of the liquid aluminum. Its volume fraction was 11% and its density was 279kg/m^3 . Temperature-dependent material properties of $AlSi_7$ were extracted from [29]. The Al-foam was processed using slitting cutters and end mill tools. Test specimens were cut to a length, width and thickness of 100mm, 35mm and 10mm, respectively.

A GSI-Lumonics 2kW Nd:Yag laser was used with a minimum spot size of 1mm and a wavelength of 1064nm. The specimens were clamped onto a 6 degree-of-freedom Stäubli RX1300 robot and scanned underneath the laser source as shown in Fig. 4. A long-wavelength infrared camera with a maximum frame rate of 120Hz was used to generate close-up thermal measurements. A specimen holder stage was made that

allowed mounting the IR camera below and on the top of the specimen. The top surface was imaged at a 45° angle to prevent the IR camera from interfering with the laser.

Stationary laser experiments were performed at 30W using a defocused laser beam with a 6mm radius. The laser center was aimed at cell wall intersections to minimize the amount of radiation absorbed within the cavities. During the laser application, the top and bottom temperature distributions were measured in real time at 120Hz. The tests were repeated at multiple locations on several specimens to statistically account for the irregularities in the foam structure.

Laser scan experiments were performed at 50W using a defocused laser beam radius of 6mm. The specimens were scanned across the entire width at scanning speeds of 2.5mm/s, 3.33mm/s and 5mm/s. The temperatures were again measured in real time at 120Hz on the top and bottom surfaces. The specimens were scanned in the x-direction close to the center of the specimen. Multiple scans were performed on several specimens, and for each scan the y-position was varied slightly.

4. RESULTS & DISCUSSION

4.1 Thermal Imager Calibration

Aluminum is a grey body with a low emissivity, and its emissivity can change dramatically as a function of position, surface texture and temperature. In order to minimize the uncertainty in the emissivity value, the test specimens were coated with black graphite paint, which is a material known to have a very high emissivity. To measure the emissivity of the graphite paint, a coated aluminum specimen was heated to 100°C, 200°C, 300°C and 400°C in a tube furnace, and the emissivity value in the IR

camera was adjusted until the measured temperature matched the furnace temperature. The emissivity remained constant at 0.92 for all temperatures. As a result, a constant emissivity of 0.92 was used for all experiments.

The spatial resolution of the IR camera is limited to the smallest area a single pixel can detect. This was calculated to be $0.05\text{mm}\times 0.05\text{mm}$ for a 23° lens operated at a minimum measurement distance of 20mm. Since the average foam wall thickness was approximately $85\mu\text{m}$, the spatial resolution was sufficient to detect most of the geometrical details.

The IR camera response time was tested by imaging a high-speed steel sheet forming process at powers of 800W (high) and 400W (low) with scanning speeds 50mm/s and 25mm/s, respectively. The temperature was measured on the top surface. Since the camera measurement range was limited to $150\text{-}900^\circ\text{C}$, the experimental results were extrapolated below 150°C . Figure 5 shows a comparison between the experimental results and numerical results that were generated with a model that was used in previous studies by Li et al. [5] and Bao et al. [30]. The numerical model could be used as a reference since it had been validated by comparing the simulated bending angles with experimentally measured bending angles. A very good agreement was achieved between the simulation and the experiment, indicating that the camera response time is sufficient to capture transient temperature phenomena during laser forming processes.

4.2 Stationary Heating Source

For laser forming of solid materials, power levels are normally chosen such that the maximum temperature in the material is just below the melting temperature. In foam materials, however, power levels need to be chosen more conservatively since thin cell walls melt very easily. To ensure that no melting occurs, a low power of 30W was used with a large defocused laser beam radius of 6mm. Note that in Secs. 4.2 and 4.3, only the Kelvin-cell model was used for the numerical simulations. Since the Kelvin-cell model represents a good middle ground between the simplicity of the equivalent model and the complexity of the voxel model, it was used representatively for all the numerical models. The comparison between the three models will be performed in Sec. 4.5.

Figures 6(a) and 6(b) show the experimental and numerical temperature distribution on the top surface. The top surface was imaged at an angle of 45° after the completion of the 2s pulse at 30W. In general, a good agreement was achieved between the experimental and numerical color contours. Figures 6(c) and 6(d) show the corresponding experimental and numerical color contours on the bottom surface. In the experiment, the maximum temperature magnitudes were slightly higher than the numerical ones, which can be attributed to the geometrical assumptions of the Kelvin-cell model. In the real foam, the cell walls were very thin and were oriented almost perfectly perpendicular to the top surface. As a consequence, the laser irradiation was mostly absorbed within the cavities, and the heat could easily conduct to the bottom of the specimen. In the Kelvin-cell model on the other hand, the cell walls were thicker (since the thickness was constant in the entire model) and the cell walls were oriented

at an angle relative to the top surface (see Sec. 4.5). Therefore, the cell walls could absorb a majority of the incoming heat flux, and the heat needed to conduct through a greater distance to reach the bottom surface. This discrepancy in the absorption could be remedied by using spherical cavities as was done by Zhang et al. [17]. However, the minimum volume fraction of spherical cavity models is around 27%, which is much higher than the 11% volume fraction of the foam that was used in this study. The volume fraction could potentially be reduced by randomizing the cavity geometry, size and orientation as was done for ellipsoidal cavities by De Giorgi et al. [27]. Yet, that approach significantly increases the model complexity and thus reduces the benefit of using an approximate geometry. It can be concluded that the Kelvin-cell model has the advantage of achieving a volume fraction of precisely 11% while being rather simple to model, but it comes at the cost of a rather crude geometrical approximation.

Figure 7 shows the experimental and numerical radial temperature distributions on the top surface after 0.5s, 1s and 2s during the laser pulse. In both the experiment and the simulation the temperature distribution maintained the same profile throughout the laser pulse, which approximately mirrored the Gaussian profile of the incoming laser irradiation. During the laser pulse, the temperature profile simply shifted up, indicating that the material underwent uniform heating throughout the pulse.

Figure 8 shows the experimental and numerical temperature history on the top and bottom surface during the 2s laser pulse. It also shows the transient temperature gradient that was calculated by subtracting the bottom temperature from the top temperature. Overall, a very good agreement was achieved between the experimental

and numerical results for the top, bottom and the gradient. The bottom numerical temperature was again slightly lower than the experimental one for the same reason that was explained earlier. As a consequence, the Kelvin-cell model slightly overestimated the gradient. From both the experiment and the simulation it is evident that a steep temperature gradient develops quickly when Al-foam is subjected to a laser pulse. The experimental and numerical time constants of the gradient were 0.18s and 0.2s, respectively. It can further be observed that the bottom temperature rise was delayed relative to the top. Interestingly, once the bottom temperature started to rise, it kept rising at the same rate as the top, such that a constant gradient was maintained throughout the rest of the laser exposure.

4.3 Moving Heating Source

Figures 9(a) and 9(b) show the top experimental and numerical temperature history plots during laser scans at 50W with a 6mm radius at scanning speeds 2.5mm/s, 3.33mm/s and 5mm/s. Note that the laser powers had to be kept low to prevent thin cell structures from melting, as explained in Sec. 4.2. In order to maintain similar line energies as in solid laser forming, the scanning speeds had to be reduced as well. Further note that the experimental plots were extrapolated below 150°C due to the camera range limit. To explain these results, two phenomena need to be discussed that occur when the laser scanning speed is increased. Firstly, the incoming heat flux is reduced since the material is subjected to the laser for a shorter amount of time. Secondly, there is less time for the heat to diffuse away from the top surface, as shown by Li et al. [5]. These phenomena work against each other since the former decreases

the top temperature while the latter increases it. As can be seen in Figs. 9(a) and 9(b), the first phenomenon was dominant in the experiment because the temperature increased significantly with decreasing scanning speed. In the simulation on the other hand, the temperature difference was much smaller, indicating that the second phenomenon was dominant. This discrepancy is related to the difference in the absorption that was explained in Sec. 4.2. In the experiment, the heat could quickly diffuse to the bottom, even at elevated scanning speeds. In the Kelvin-cell model, on the other hand, the heat remained trapped close to the top surface. At higher scanning speeds, the heat was unable to diffuse away quickly, and the temperature therefore increased substantially. The bottom temperature history plots of Figs. 9(c) and 9(d) confirm these observations since the experimental temperatures were much greater than the numerical ones.

Figure 10 shows the maximum experimental and numerical temperature gradients during a 50W laser scan at 2.5mm/s, 3.33mm/s and 5mm/s. The gradients were obtained by subtracting the bottom temperature distributions from the top temperature distributions and extracting the maximum values. The experimental and numerical gradients differed in magnitude since the numerical bottom temperatures in Fig. 9 were lower than the experimental bottom temperatures. In both the experiment and the simulation, the gradient decreased with increasing scanning speed. This result is intuitive because the gradient had less time to establish with increasing scanning speed. Moreover, it is obvious from the results in Fig. 9 that the decrease in the top

temperature with increasing speed was greater than the corresponding decrease in the bottom temperature.

4.4 Fourier Number

In laser forming of solid metals, three bending mechanisms have been identified, which are the temperature gradient mechanism (TGM), buckling mechanism (BM) and upsetting mechanism (UM) [31]. Moreover, the Fourier number was found to be a good indicator of which bending mechanism is dominant. It can be expressed as

$$Fo = \frac{D\alpha}{vt^2} \quad (6)$$

where D is the laser diameter, α is the foam thermal diffusivity, v is the laser scanning speed and t is the sheet thickness. For $Fo < 1$, TGM is expected to be the dominating mechanism, whereas $Fo > 1$ indicates that BM or UM are the dominating mechanisms. In order to determine whether the same threshold is valid for foams, the foam Fourier numbers need to be compared to the corresponding solid Fourier numbers. In foams, the laser diameters are generally bigger and the scanning speeds are lower than in solids since the laser power needs to be kept low. At the same time, foams have much smaller thermal diffusivities compared to solids, while foam sheet thicknesses are comparatively larger. Since the Fourier number is inversely proportional to the square of the thickness and only linearly dependent on the remaining variables, the Fourier numbers of foams should generally be lower than the corresponding solid Fourier numbers. Thus, based on this analysis TGM should always be the dominant bending mechanism.

Moreover, even if the Fourier number was greater than 1, BM and UM could not occur in foams. In order for BM and UM to be dominant, the material needs to be able to develop high compressive stresses to allow buckling or thickening. Due to the thin cell walls, however, foams crush before such high compressive stresses can develop. Therefore, it is not necessary to specify a threshold on the Fourier number since TGM is the only possible bending mechanism for foams.

4.5 Numerical Model Comparison

In this section, the equivalent, Kelvin-cell and voxel models are compared with each other and with experimental results. Before starting the comparison, several comments need to be made about the equivalent model. Since equivalent models use a simple solid geometry, extreme care needs to be taken in the determination of the equivalent thermal conductivity. The three different approaches introduced in the background were contrasted. The Voronoi-structure method and the visual method yielded shape factors of 0.43 and 0.46, which resulted in equivalent thermal conductivities of $k_{eq}=8.1\text{W/mK}$ and $k_{eq}=8.7\text{W/mK}$, respectively. The experimentally tuned equivalent thermal conductivity turned out to be $k_{eq}=10.5\text{W/mK}$. Thus, there was a rather significant disparity in the results, which is based on the underlying assumptions of the different methods. In the Voronoi-structure method, it was assumed that the foam structure could be approximated by randomly oriented honeycombs with constant wall thicknesses. Since solid aluminum is accumulated between cavities in the actual foam, the geometrical approximations in the Voronoi-structure were still too crude despite the randomized cell distribution. A higher level of accuracy was achieved with the visual

method in which the cell wall areas and the cell wall orientations were taken into account. However, the model accuracy was still limited since the mass distribution was not taken into account. This becomes clear from the fact that the visual method would predict the same shape factors for foams with huge and tiny cells as long as their cell walls have the same overall area and average orientation. In this specific case, the experimentally tuned thermal conductivity yielded the best results since it was directly tuned with laser-forming thermal data. Overall, this comparison emphasized that the choice of the equivalent thermal conductivity evaluation method has a high impact on the performance of the equivalent model, especially for foams with small solid volume fractions.

Figure 11 shows typical color contour plots of the equivalent, Kelvin-cell and voxel model during a laser scan. In the equivalent model, all the incoming laser irradiation was absorbed at the top surface ($z=10\text{mm}$). Therefore, heating was extremely localized and the isotherms were very shallow close to the top surface. Moreover, the isotherms were rather wide in the x and y -direction, indicating that the heat could easily escape along the side of the specimen. As a consequence, less heat could reach the bottom surface, and the temperature magnitude on the bottom surface was reduced. In the Kelvin-cell model, the laser irradiation could penetrate into the material, which caused the isotherms to be spaced farther apart in the z -direction. Yet, since the cell walls were oriented at an angle at the top surface, a majority of the incoming heat flux was still absorbed close to the top surface. In the voxel model, the laser could penetrate deeply into the material since the thin cell walls were almost perpendicular to the top surface.

As a consequence, the heat flux was mainly absorbed inside the cavities. The isotherms were thus spaced further apart in the z -direction, indicating that more heat could reach the bottom surface. Overall, the temperature distribution of the voxel model was most realistic, while the equivalent model induced significant errors due to inaccurate top surface boundary conditions.

Figure 12 shows the cross-sectional heat flux vectors of the different numerical models during a laser scan. The figure nicely illustrates the differences in the absorption schemes that were discussed in Fig. 11. In the equivalent model, the heat was absorbed entirely at the top surface ($z=10\text{mm}$), while in the voxel model the heat could penetrate even further into the material than in the Kelvin-cell model due to the different cell wall orientations and thicknesses. The figure further illustrates differences in the heat flow patterns. In the equivalent model, the heat could diffuse away radially from the top surface, which overestimated the heat transfer in y -direction and underestimated the heat transfer to the bottom surface. In the explicit porous models on the other hand, the heat was channeled through the thin cell walls since it was assumed that the heat transfer through the cavities is negligible. As a consequence, the topmost cavities created a barrier for the heat transfer in the y -direction, and less heat could escape along the side of the specimen. In the voxel model, the heat flow was additionally obstructed in locations where cell walls were interrupted or of a small thickness. Thus, the voxel model again provided the most realistic heat flow simulation since it contained the highest level of geometrical details.

Figure 13 compares the top and bottom temperature history plots of the experiment and the three numerical models during a 2s laser pulse with a 6mm radius at 30W. On the top surface, the Kelvin-cell model and the equivalent model agreed well with the experimental results. In the voxel model, however, the temperature rise was delayed. This discrepancy can be related to the surface geometry of the voxel model. During the voxel model generation, each data point of the CT-scan was converted to a cubical element, called a voxel. As a consequence, the surface of the voxel model had a staircase structure, which overestimated the surface area and hence the convective heat losses. Due to the increased convective losses, the rise in the temperature was delayed. On the bottom surface, the equivalent model predicted a very small temperature rise, which is related to the fact that the entire laser irradiation was absorbed at the top surface as shown previously. The Kelvin-cell and voxel model predictions were much closer to the experimental results, which is again consistent with the previous findings. Overall, the differences between the three models could be mostly attributed to the laser absorption boundary condition on the top surface. If the specimen thickness was increased or the cavity size was reduced, the influence of the top surface boundary condition would be reduced, and thus the three models would yield more similar results.

The results from Fig. 13 can be used to predict the amount of bending that each model will generate in a thermo-mechanical analysis. Previous studies [5,6] have shown that the bending angle is proportional to the temperature gradient. Therefore, the

equivalent model is expected to yield the highest bending angles, whereas the explicit porous models are expected to generate smaller bending angles.

Figure 14 compares the experimental temperature history plots with the numerical plots for a 50W laser scan with a beam radius of 6mm and at a scanning speed 5mm/s. The equivalent and Kelvin-cell models yielded similar heating and cooling rates as the experiment. In the voxel model, the heating and cooling rates were slightly reduced due to the overestimation of convective losses as mentioned previously. In the Kelvin-cell model, the temperature magnitudes were slightly higher than in the experiment as was explained in Sec. 4.3.

Figure 15 shows the maximum experimental and numerical temperatures during 50W scans at 2.5mm/s, 3.33mm/s and 5mm/s. All the numerical models predicted a linear decrease in the maximum temperature with increasing scanning speeds. In the experimental results the trend was not perfectly linear since the standard deviations were rather large. The voxel model was the only model that was able to capture the full temperature drop with increasing scanning speed. This reflects the fact that the temperature distributions and the heat flow patterns of the voxel model were most realistic. The Kelvin-cell and the equivalent model, on the other hand, both underestimated the temperature drop. The equivalent model performed slightly better than the Kelvin-cell model since the heat was able to escape in the y-direction along the side of the specimen. In the Kelvin-cell model, the heat remained trapped close to the top surface and could neither escape through the bottom nor the side. Hence, the temperatures could rise rather high despite the increase in the scanning speed.

5. CONCLUSIONS

The equivalent, Kelvin-cell and voxel models all predicted steep temperature gradients during laser forming of Al-foam, and this result was both validated by experiments and theory. The advantages and disadvantages of the three numerical models were evaluated. The equivalent model was extremely simple to generate, but introduced significant errors due to the assumption that the entire heat flux is absorbed at the top surface. As a consequence, this model underestimated the bottom surface temperature, which in turn led to a higher predicted temperature gradient. Due to the crude geometrical structure of the equivalent model, the specification of the equivalent material properties was crucial, especially since the solid volume fraction was low. In comparison, the Kelvin-cell model was able to replicate the exact volume fraction of the real foam without significantly increasing the model complexity. Due to the accuracy in the volume fraction, a good agreement was achieved with the experiment for the response to stationary laser sources. At the same time, the shape of the Kelvin-cells overestimated the laser absorption close to the top surface, which limited its response to changes in laser scanning speeds. Finally, the voxel model could replicate the exact foam geometry, which allowed for the most accurate temperature distributions and heat flow predictions during the laser exposure. As a consequence, the model was highly responsive to changes in processing conditions. The drawbacks of the voxel model were that it was computationally intensive and the staircase structure of its surface caused an overestimation of the surface area and therefore the convective losses.

ACKNOWLEDGMENT

Financial support from Columbia University is acknowledged. In addition, the authors acknowledge the support of Bin Zhou and the Bone Bioengineering Lab at Columbia University during the generation of the CT-scan and the voxel FEM model.

NOMENCLATURE

Gr	Grashof number
g	Gravitational constant
β	Volumetric expansion coefficient
ΔT_c	Maximum temperature gradient over a single cavity
T_{avg}	Average temperature
d	Cavity diameter
μ_g	Dynamic viscosity of the gas
ε	Emissivity
σ	Boltzmann constant
k_{eq}	Equivalent thermal conductivity
k_s	Solid thermal conductivity
k_{rad}	Radiative thermal conductivity
ρ_g	Gas density
ρ_s	Solid density
ρ_f	Foam density
t	Sheet thickness
f_z	Shape factor

A_i	Cross-sectional areas of cell walls
γ_i	Angular orientations of cell walls
q	Heat flux
Fo	Fourier number
D	Laser diameter
α	Thermal diffusivity
v	Laser scanning speed

REFERENCES

1. Fuganti, A., Lorenzi, L., Hanssen, A. G., and Langseth, M., 2000, "Aluminium Foam for Automotive Applications," *Adv. Eng. Mater.*, **4**(2), pp. 200-204.
2. Davim, J. P., 2012, *Lasers in Manufacturing*, Wiley-ISTE, London.
3. Contorno, D., Filice, L., Fratini, L., and Micari, F., 2006, "Forming of Aluminum Foam Sandwich Panels: Numerical Simulations and Experimental Tests," *J. Mater. Process. Technol.*, **177**(1-3), pp. 364-367.
4. Zu, G. Y., Lu, R. H., Li, X. B., Zhong, Z. Y., Ma, X. J., Han, M. B., and Yao, G. C., 2013, "Three-point Bending Behavior of Aluminum Foam Sandwich with Steel Panel," *Trans. Nonferrous. Met. Soc. China*, **23**(9), pp. 2491-2495.
5. Li, W., and Yao, Y. L., 2001, "Laser Forming with Constant Line Energy," *Int. J. Adv. Manuf. Technol.*, **17**(3), pp. 196-203.
6. Li, W., and Yao, Y. L., 2000, "Numerical and Experimental Study of Strain Rate Effects in Laser Forming," *ASME J. Manuf. Sci. Eng.*, **122**, pp. 445-451.
7. Cheng, J., and Yao, Y. L., 2001, "Cooling Effects in Multiscan Laser Forming," *SME J. Manuf. Processes*, **3**(1), pp. 60-72.
8. Cheng, J., and Yao, Y. L., 2002, "Microstructure Integrated Modeling of Multiscan Laser Forming," *ASME J. Manuf. Sci. Eng.*, **124**, pp. 379-388.
9. Cheng, P., Fan, Y., Zhang, J., Mika, D., Graham, M., Zhang, W., Marte, J., Jones, M., Yao, Y. L., 2006, "Laser Forming of Varying Thickness Plate – Part I: Process Analysis," *ASME J. Manuf. Sci. Eng.*, **128**, pp. 634-641.
10. Cheng, J., and Yao, Y. L., 2004, "Process Synthesis of Laser Forming by Genetic Algorithms," *Int. J. Mach. Tool. Manu.*, **44**(15), pp. 1619-1628.
11. Guglielmotti, A., Quadrini, F., Squeo, E. A., and Tagliaferri, V., 2009, "Laser Bending of Aluminum Foam Sandwich Panels," *Adv. Eng. Mater.*, **11**(11), pp. 902-906.
12. Quadrini, F., Guglielmotti, A., Squeo, E. A., and Tagliaferri, V., 2010, "Laser Forming of Open-Cell Aluminium Foams," *J. Mater. Process. Technol.*, **210**(11), pp. 1517-1522.
13. Santo, L., Guglielmotti, A., and Quadrini, F., 2010, "Formability of Open-Cell Aluminium Foams by Laser," *ASME Paper No. MSEC2010-34282*, pp. 265-272.
14. Quadrini, F., Bellisario, D., Ferrari, D., Santo, L., and Santarsiero, A., 2013, "Numerical Simulation of Laser Bending of Aluminum Foams," *Key Eng. Mater.*, **554-557**, pp. 1864-1871.
15. Santo, L., Bellisario, D., Rovatti, L., and Quadrini, F., 2012, "Microstructural Modification of Laser-Bent Open-Cell Aluminum Foams," *Key Eng. Mater.*, **504-506**, pp. 1213-1218.
16. Quadrini, F., Bellisario, D., Ferrari, D., Santo, L., and Santarsiero, A., 2014, "Numerical Simulation of Laser Forming of Aluminum Sponges: Effect of Temperature and Heat Treatments," *Key Eng. Mater.*, **611-612**, pp. 731-738.
17. Zhang, M., Chen, C. J., Brandal, G., Bian, D., and Yao, Y. L., 2015, "Experimental and Numerical Investigation of Laser Forming of Closed-Cell Aluminum Foam," *ASME J. Manuf. Sci. Eng.*, **138**(2), p. 021006.
18. MacGregor, R. K., and Emery, A. F., 1969, "Free Convection Through Vertical Plane Layers – Moderate and High Prandtl Number Fluids," *ASME J. Heat Trans.*, **91**(3), p. 391.

19. Gibson, L. J., and Ashby, M. F., 1988, *Cellular Solids: Structure and Properties*, Pergamon, Oxford.
20. Mukarami, T., Tsumura, T., Ikeda, T., Nakajima, H., and Nakata, K., 2007, "Anisotropic Fusion Profile and Joint Strength of Lotus-Type Porous Magnesium by Laser Welding," *Mater. Sci. Eng. A*, **456**(1-2), pp. 278-285.
21. Yilbas, B. S., Akhtar, S. S., and Keles, O., 2013, "Laser Cutting of Aluminum Foam: Experimental and Model Studies," *ASME J. Manuf. Sci. Eng.*, **135**(5), p.051018.
22. Ashby, M. F., Evans, A. G., Fleck, N. A., Gibson, L. J., Hutchinson, J. W., and Wadley, H. N. G., 2000, *Metal Foams: A Design Guide*, Butterworth-Heinemann, Washington DC.
23. Öchsner, A., Murch, G. E., and De Lemos, M. J. S., 2008, *Thermal Properties Simulation and Prediction*, Wiley-VCH, Weinheim.
24. Randrianalisoa, J., and Baillis, D., 2014, "Thermal Conductive and Radiative Properties of Solid Foams: Traditional and Recent Advanced Modelling Approaches," *C. R. Phys.*, **15**(8-9), pp. 683-695.
25. Lu, T. J., and Chen, C., 1999, "Thermal Transport and Fire Retardance Properties of Cellular Aluminium Alloys," *Acta Mater.*, **47**(5), pp. 1469-1485.
26. Ma, M. Y., and Ye, H., 2014, "An Image Analysis Method to Obtain the Effective Thermal Conductivity of Metallic Foams via a Redefined Concept of Shape Factor," *J. Appl. Therm. Eng.*, **73**(1), pp. 1277-1282.
27. De Giorgi, M., Carofalo, A., Dattoma, V., Nobile, R., and Palano, F., 2010, "Aluminium Foams Structural Modelling," *Comput. Struct.*, **88**(1-2), pp. 25-35.
28. Mills, N. J., Stämpfli, R., Marone, F., and Brühwiler, P. A., 2009, "Finite Element Micromechanics Model of Impact Compression of Closed-cell Polymer Foams," *Int. J. Solids Struct.*, **46**(3-4), pp. 677-697.
29. Spittel, T., Spittel, M., and Warlimont, H., 2011, *Non-ferrous Alloys – Light Metals*, Springer, Berlin, Vol. 2C2.
30. Bao, J., and Yao, Y. L., 2001, "Analysis and prediction of edge effects in laser bending," *ASME J. Manuf. Sci. Eng.*, **123**, pp. 53-61.
31. Geiger, M., and Vollertsen, F., 1993, "The Mechanisms of Laser Forming," *CIRP Ann.*, **42**(1), pp. 301-304.

Figure Captions List

- Fig. 1 Closed-cell aluminum foam specimen after laser forming
- Fig. 2 (a) Equivalent model, (b) Kelvin-cell model and (c) voxel model
- Fig. 3 Determining the equivalent thermal conductivity using the visual method by calculating the cross-sectional areas and the angular orientations of the cell walls.
- Fig. 4 Experimental setup
- Fig. 5 Experimental and numerical temperature history response during steel sheet laser forming at 800W – 50mm/s (high) and 400W – 25mm/s (low)
- Fig. 6 (a) and (c) show the experimental top and bottom temperature distributions, respectively, and (b) and (d) show the numerical (Kelvin-cell) top and bottom temperature distributions, respectively, after a 2s exposure to a 30W laser with a 6mm radius.
- Fig. 7 (a) Experimental and (b) numerical (Kelvin-cell) temperature distribution from the laser center to the edge of the laser source after a 30W laser exposure with a 6mm radius. The experimental data is averaged over 15 specimens and standard errors are shown.
- Fig. 8 (a) Experimental and (b) numerical (Kelvin-cell) temperature history plots during a 2s exposure to a 30W defocused laser beam with a 6mm radius. The experimental data is averaged over 15 specimens and standard

errors are shown.

Fig. 9 (a) and (c) show the experimental top and bottom temperature history plots, (b) and (d) show the numerical (Kelvin-cell) top and bottom temperature history plots at scanning speeds 2.5mm/s, 3.33mm/s and 5mm/s, respectively. The laser power was 50W with a beam radius of 6mm. The experimental results were averaged over 20 test runs and standard errors are shown.

Fig. 10 Experimental and numerical (Kelvin-cell) maximum temperature gradients during 50W scans with a 6mm beam radius at 2.5mm/s, 3.33mm/s and 5mm/s, respectively. Standard errors are shown for the experimental data.

Fig. 11 Typical color contours of the (a) equivalent model, (b) Kelvin-cell model and (c) voxel model during a laser scan. Legends are omitted since the color contours are used for a qualitative comparison.

Fig. 12 Heat flux vectors in cross-sections of the (a) equivalent model, (b) Kelvin-cell model and (c) voxel model during laser irradiation. Legends are omitted since the plots are used for a qualitative comparison.

Fig. 13 Experimental and numerical (equivalent, Kelvin-cell and voxel model) top and bottom surface temperature history plots during a 2s laser pulse at 30W with a defocused beam radius of 6mm.

Fig. 14 Experimental and numerical (equivalent, Kelvin-cell and voxel model) top

temperature history plots during a 50W scan at 5mm/s with a defocused beam radius of 6mm.

Fig. 15 Experimental and numerical (equivalent, Kelvin-cell and voxel model) maximum top surface temperatures during 50W laser scans at 2.5mm/s, 3.33mm/s and 5mm/s, respectively. Standard errors are shown for the experimental data.



Figure 1: Closed-cell aluminum foam specimen after laser forming

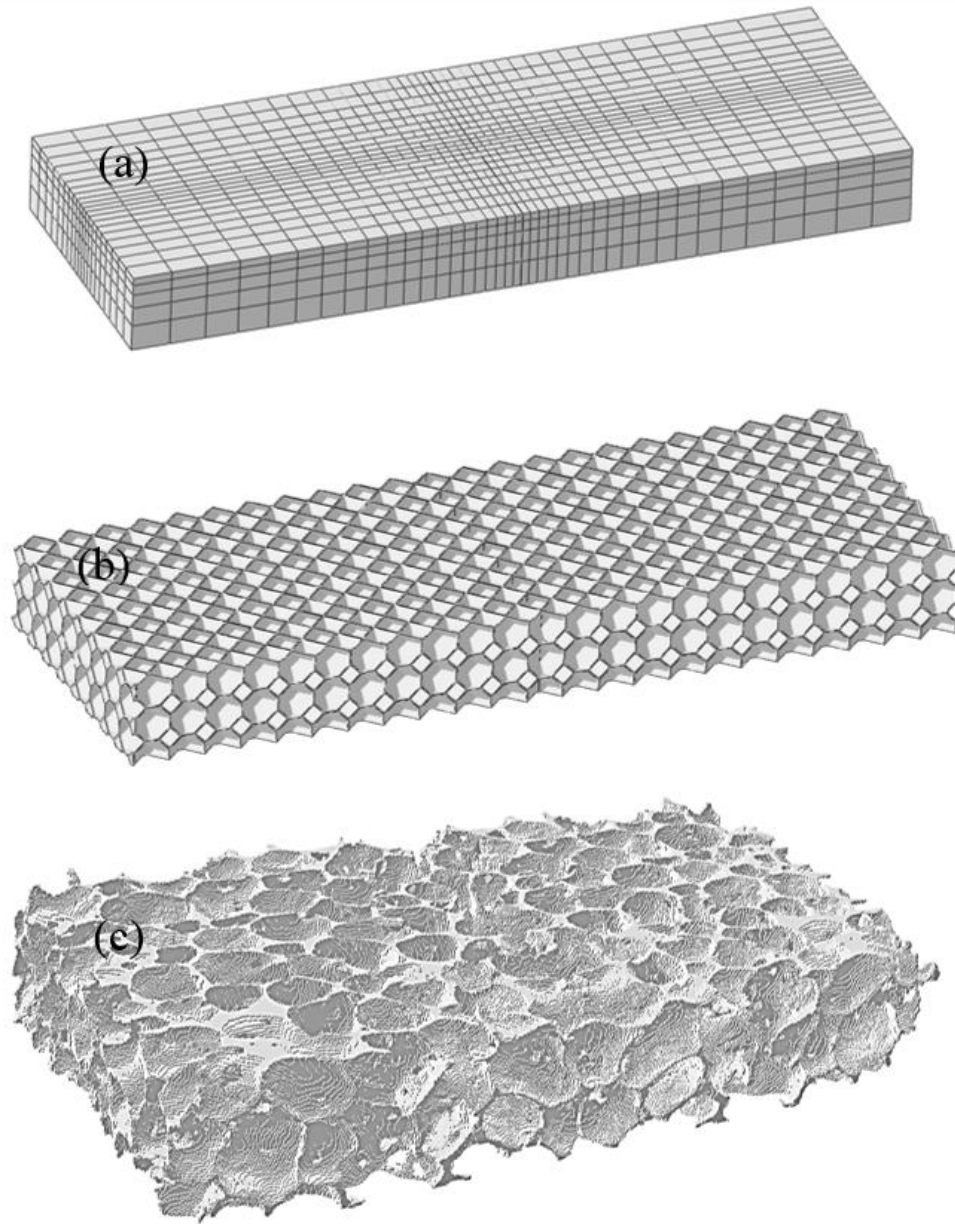


Figure 2: (a) Equivalent model, (b) Kelvin-cell model and (c) voxel model

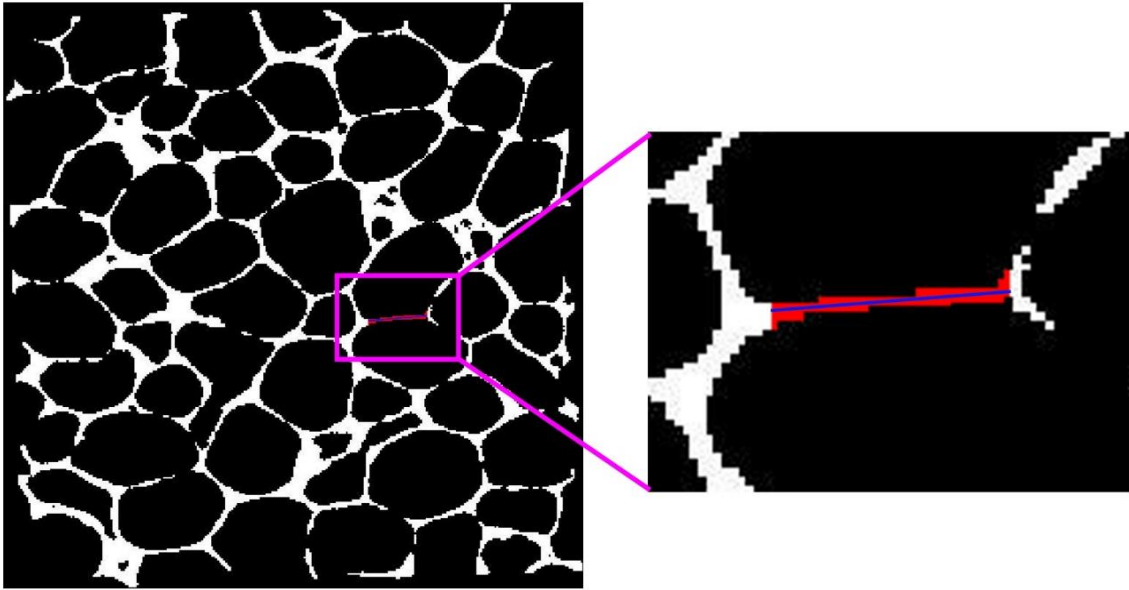


Figure 3: Determining the equivalent thermal conductivity using the visual method by calculating the cross-sectional areas and the angular orientations of the cell walls.

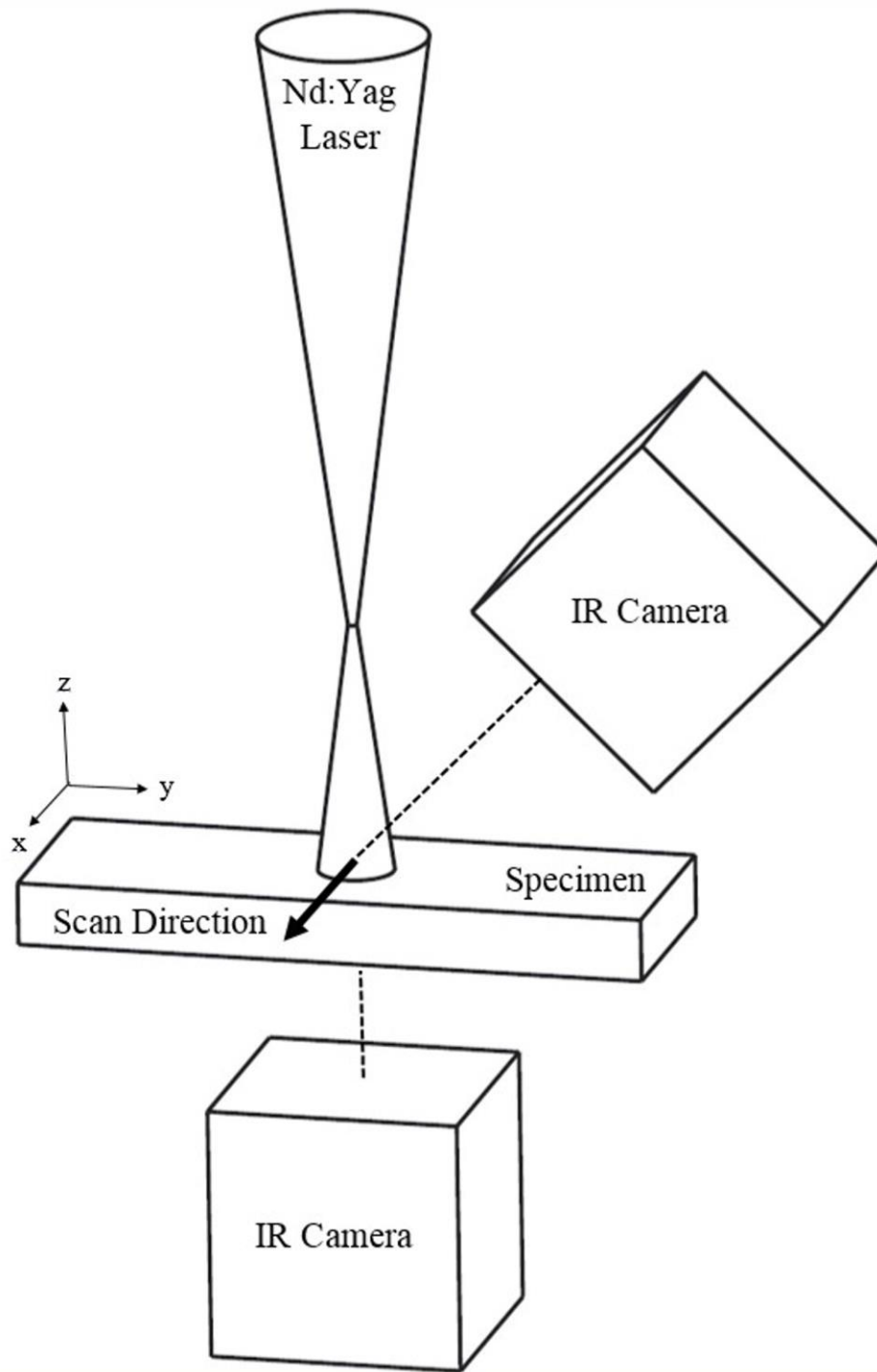


Figure 4: Experimental setup

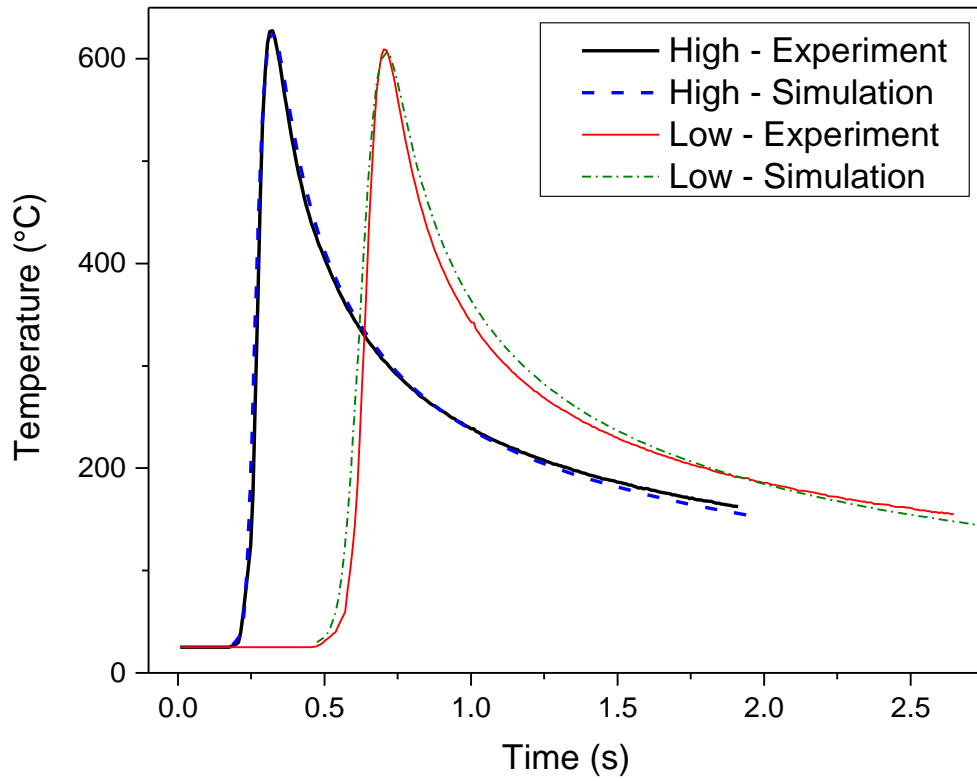


Figure 5: Experimental and numerical temperature history response during steel sheet laser forming at 800W – 50mm/s (high) and 400W – 25mm/s (low).

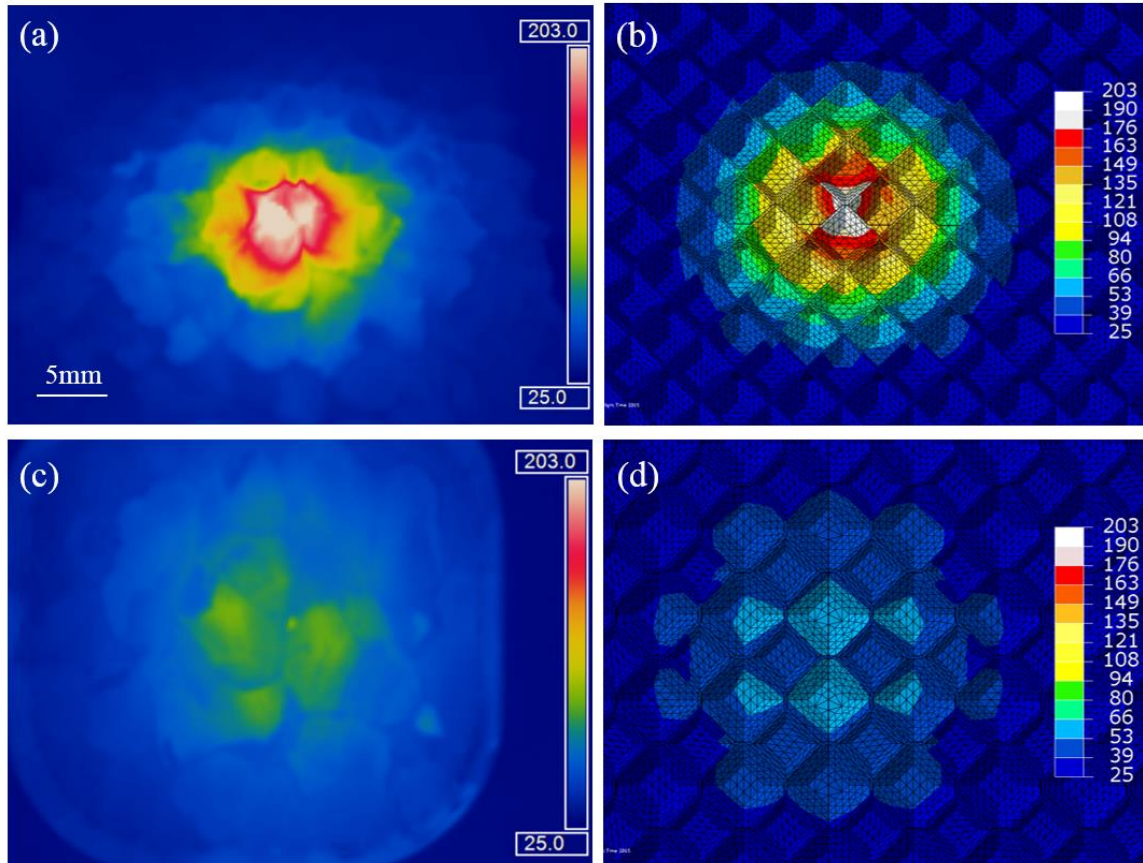


Figure 6: (a) and (c) show the experimental top and bottom temperature distributions, respectively, and (b) and (d) show the numerical (Kelvin-cell) top and bottom temperature distributions, respectively, after a 2s exposure to a 30W laser with a 6mm radius.

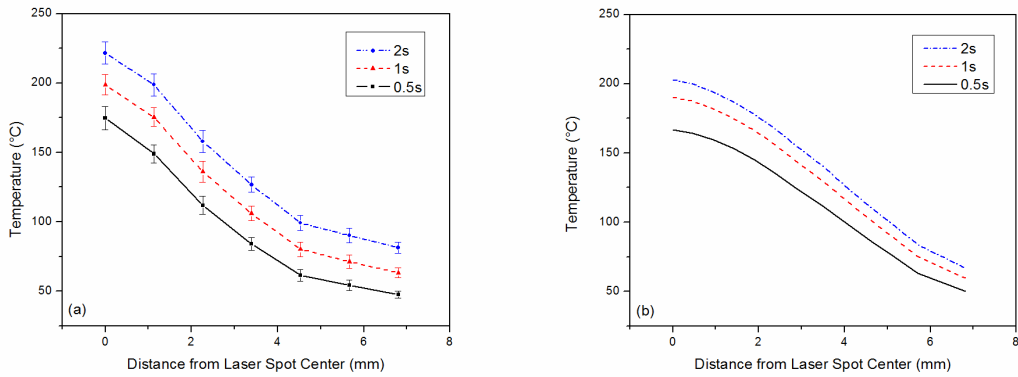


Figure 7: (a) Experimental and (b) numerical (Kelvin-cell) temperature distribution from the laser center to the edge of the laser source after a 30W laser exposure with a 6mm radius. The experimental data is averaged over 15 specimens and standard errors are shown.

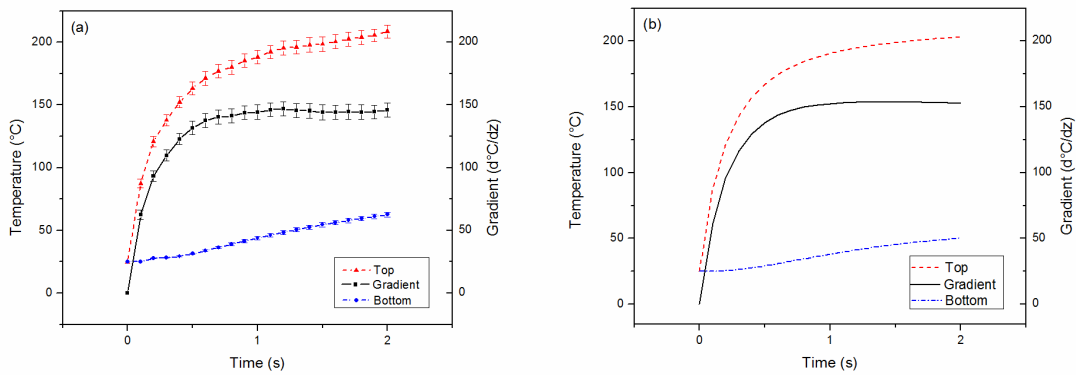


Figure 8: (a) Experimental and (b) numerical (Kelvin-cell) temperature history plots during a 2s exposure to a 30W defocused laser beam with a 6mm radius. The experimental data is averaged over 15 specimens and standard errors are shown.

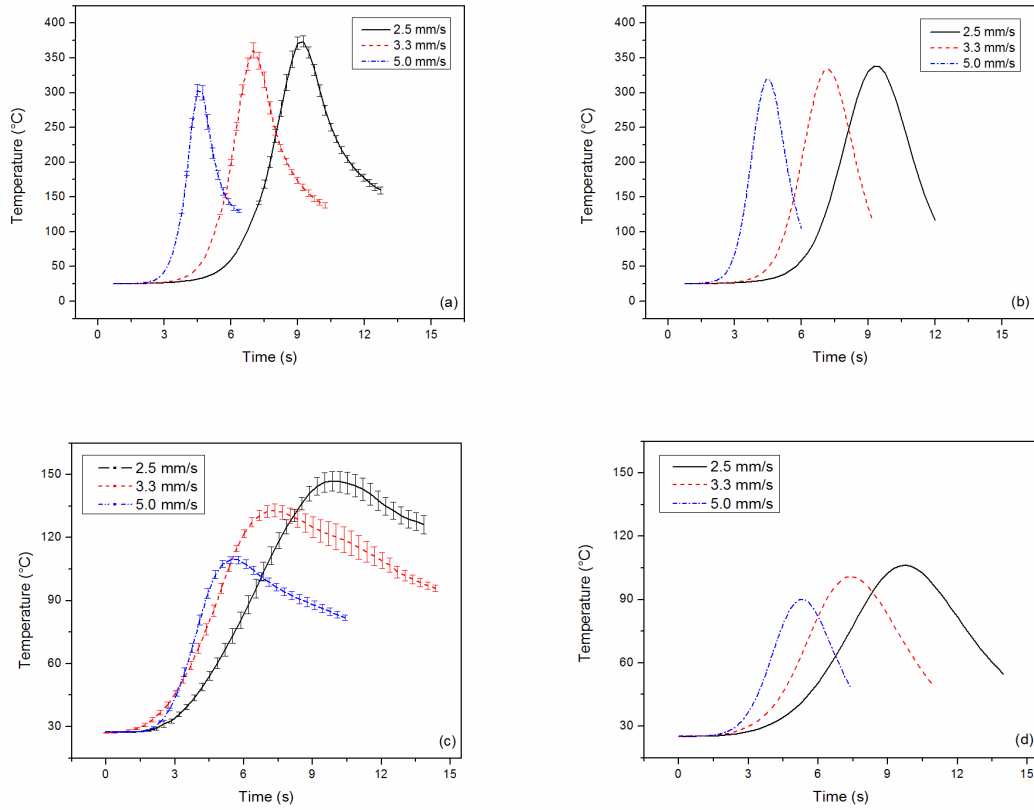


Figure 9: (a) and (c) show the experimental top and bottom temperature history plots, (b) and (d) show the numerical (Kelvin-cell) top and bottom temperature history plots at scanning speeds 2.5mm/s, 3.3mm/s and 5mm/s, respectively. The laser power was 50W with a beam radius of 6mm. The experimental results were averaged over 20 test runs and standard errors are shown.

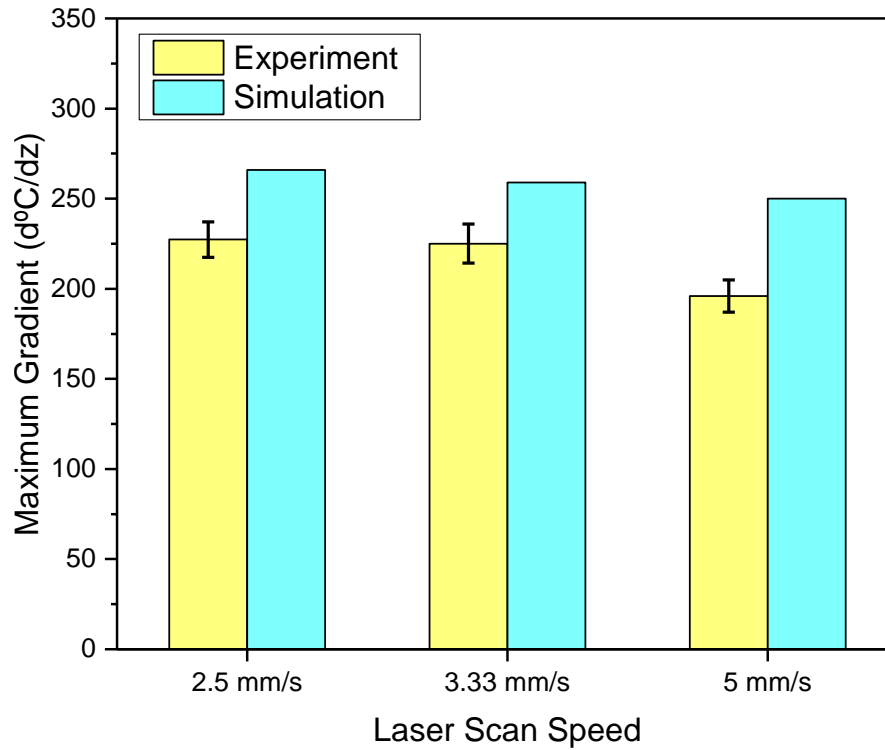


Figure 10: Experimental and numerical (Kelvin-cell) maximum temperature gradients during 50W scans with a 6mm beam radius at 2.5mm/s, 3.33mm/s and 5mm/s, respectively. Standard errors are shown for the experimental data.

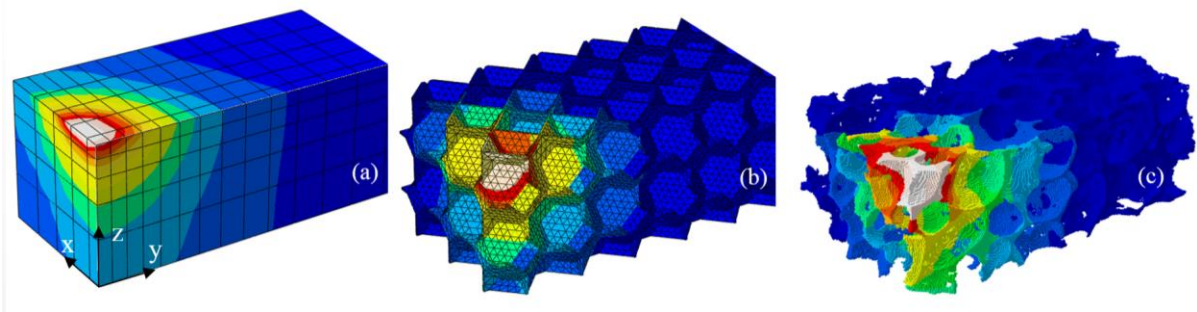


Figure 11: Typical color contours of the (a) equivalent model, (b) Kelvin-cell model and (c) voxel model during a laser scan. Legends are omitted since the color contours are used for a qualitative comparison.

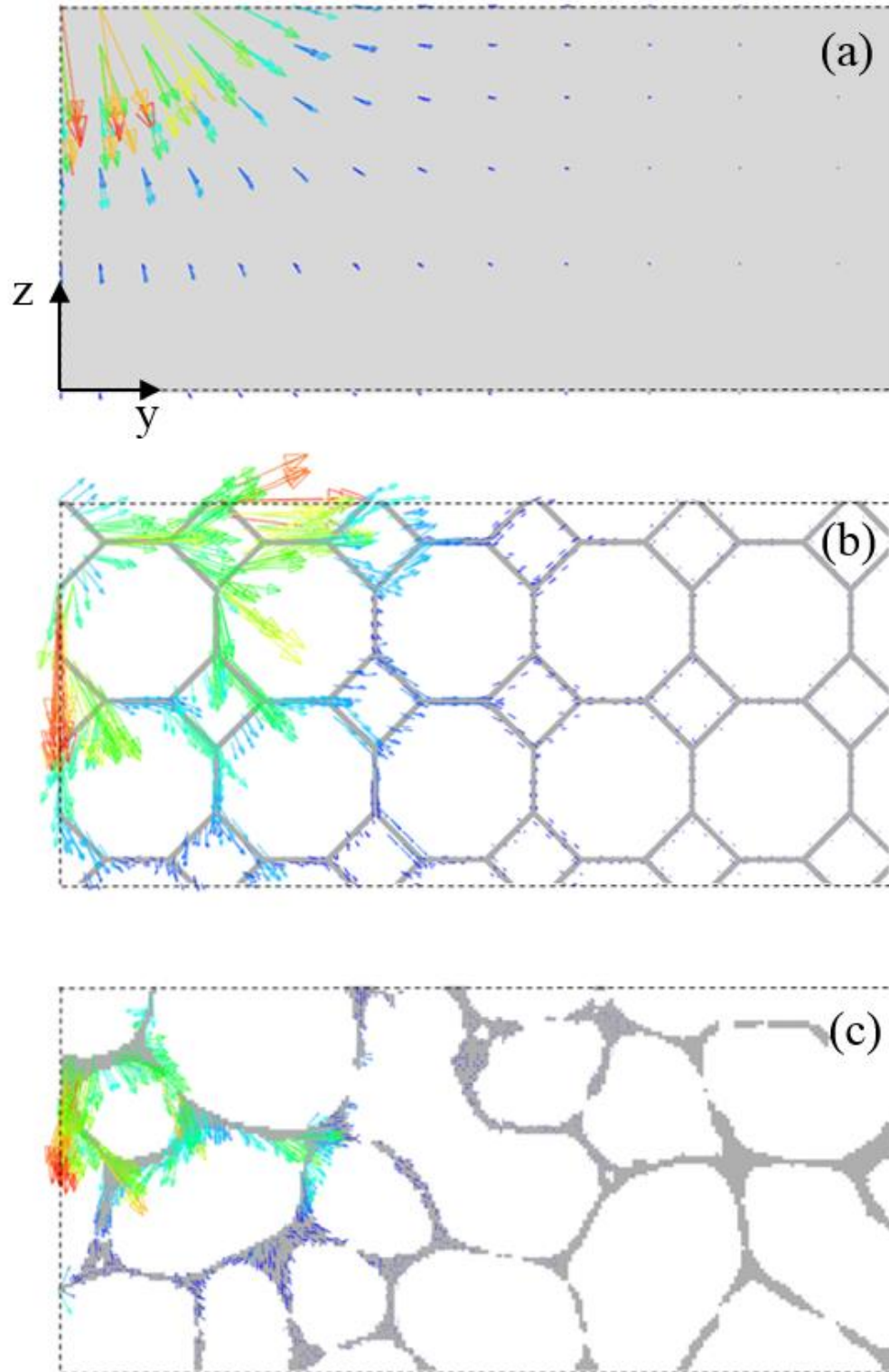


Figure 12: Heat flux vectors in cross-sections of the (a) equivalent model, (b) Kelvin-cell model and (c) voxel model during laser irradiation. Legends are omitted since the plots are used for a qualitative comparison.

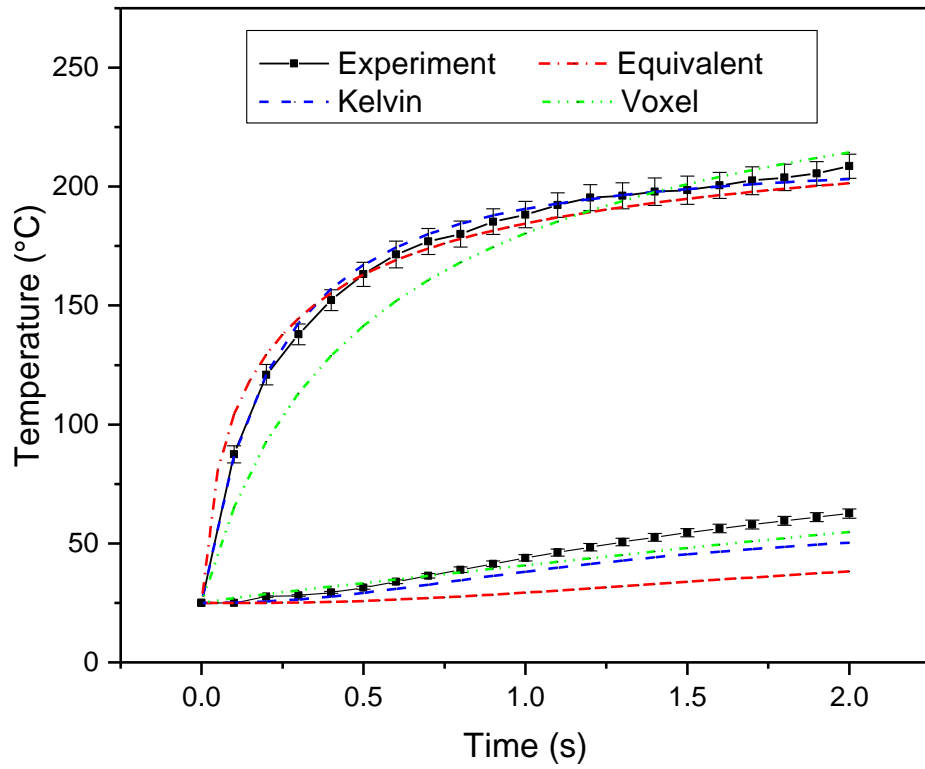


Figure 13: Experimental and numerical (equivalent, Kelvin-cell and voxel model) top and bottom surface temperature history plots during a 2s laser pulse at 30W with a defocused beam radius of 6mm.

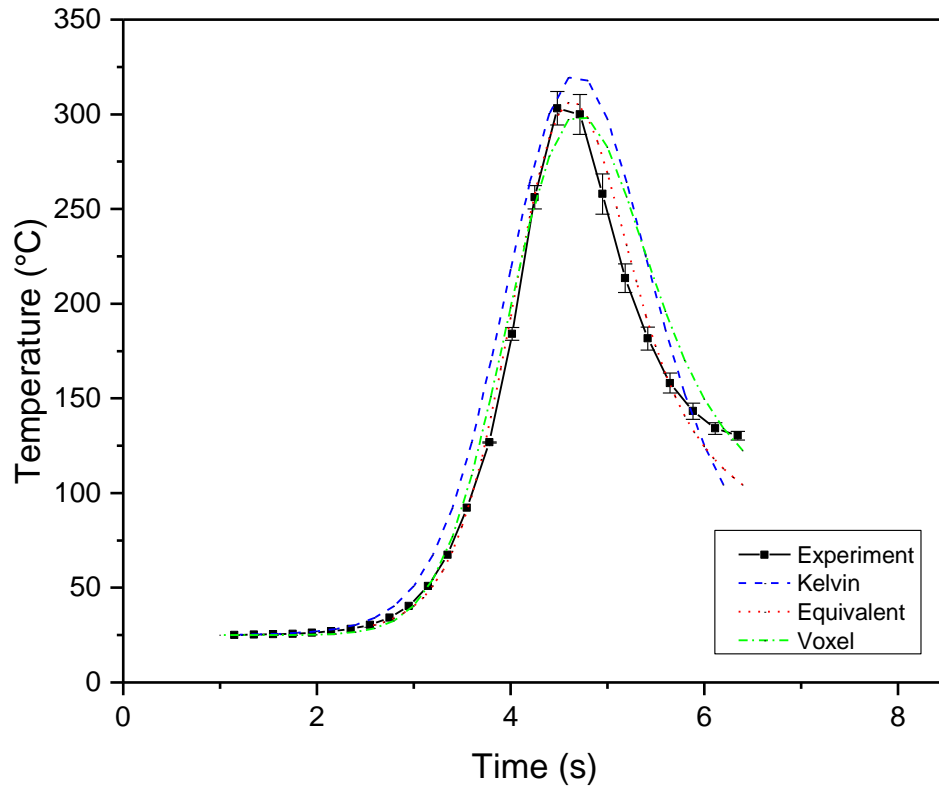


Figure 14: Experimental and numerical (equivalent, Kelvin-cell and voxel model) top temperature history plots during a 50W scan at 5mm/s with a defocused beam radius of 6mm.

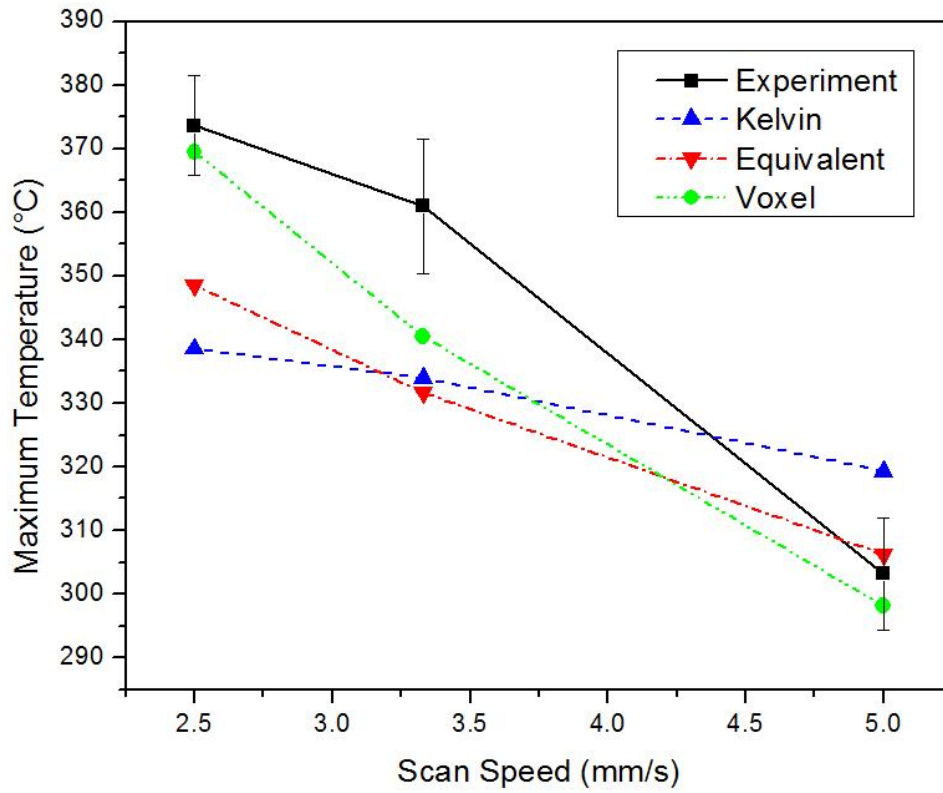


Figure 15: Experimental and numerical (equivalent, Kelvin-cell and voxel model) maximum top surface temperatures during 50W laser scans at 2.5mm/s, 3.33mm/s and 5mm/s, respectively. Standard errors are shown for the experimental data.